Atmos. Meas. Tech. Discuss., 5, 1947–1984, 2012
www.atmos-meas-tech-discuss.net/5/1947/2012/
doi:10.5194/amtd-5-1947-2012

Atmospheric Measurement Techniques Discussions

DOAS measurements of NO_2 from an ultralight aircraft during the Earth Challenge expedition

A. Merlaud[1], M. Van Roozendael[1], J. van Gent[1], C. Fayt[1], J. Maes[1], X. Toledo[2], O. Ronveaux[3], and M. De Mazière[1]

[1]Belgian Insitute for Space Aeronomy (BIRA-IASB), Avenue Circulaire 3, 1180 Brussels, Belgium
[2]University of Namur, Namur, Belgium
[3]Usf-free sky, Brussels, Belgium

Received: 21 December 2011 – Accepted: 6 February 2012 – Published: 28 February 2012

Correspondence to: A. Merlaud (alexis.merlaud@aeronomie.be)

Published by Copernicus Publications on behalf of the European Geosciences Union.

Abstract

We report on airborne Differential Optical Absorption Spectroscopy (DOAS) measurements of NO_2 tropospheric columns above South Asia, Arabic peninsula, North Africa, and Italy in November and December 2009. The DOAS instrument was installed on an ultralight aircraft involved in the Earth Challenge project, an expedition of seven pilots flying on four ultralight aircraft between Australia and Belgium. The instrument recorded spectra in limb geometry with a large field-of-view, a set-up which provides a high sensitivity to the boundary layer NO_2 while minimizing the uncertainties related to the attitude variations. We compare our measurements with OMI and GOME-2 tropospheric NO_2 products when the latter are available. Above Rajasthan and the Po Valley, two areas where the NO_2 field is homogeneous, data sets agree very well. Our measurements in this areas are respectively 0.1 ± 0.1 to $2.8 \pm 1 \times 10^{15}$ molec cm^{-2} and $2.5 \pm 0.5 \times 10^{16}$ molec cm^{-2}. Flying downwind of Riyadh, our NO_2 measurements show with a higher spatial resolution than OMI the structure of the megacities'exhaust plume. Moreover, our measurements indicate larger columns (up to 70 %) than the one seen by satellites. We also derived tropopsheric columns when no satellite data was available, if it was possible to get information on the visibility from satellite measurements of aerosol optical thickness. The maximum column we measured was above Benghazi, with $5.7 \pm 2 \times 10^{16}$ molec cm^{-2}. This experiment also provides a confirmation for the recent finding of a soil signature above desert.

1 Introduction

Nitrogen dioxide (NO_2) is both a key species in atmospheric chemistry, through its role in ozone's cycle, and an indicator of air quality. In the troposphere, its main sources are anthropogenic and related to fossil fuel combustion in car engines, thermal power stations and industries (Jacob, 1999). NO_2 contributes to the photochemical smog seen

AMTD
5, 1947–1984, 2012

above many cities and its effects on health have motivated the definition of acceptable exposure thresholds. The World Health Organization (WHO, 2003) recommends a maximum 1-hour concentration of 200 $\mu g\,m^{-3}$ and an annual average of 40 $\mu g\,m^{-3}$. In this paper we present airborne DOAS NO_2 measurements during an ultralight aircraft expedition from Thailand to Belgium during November and December 2009.

The tropospheric NO_2 loading can be remotely retrieved using its absorption band in the UV-Visible and the DOAS technique (Platt and Stutz, 2008). This is achieved from space by nadir-looking satellite-borne sensors like OMI (Levelt et al., 2006) or GOME-2 (Munro et al., 2006). These measurements are particularly valuable since they offer a global picture of the NO_2 field. However, their spatial resolution is limited by the pixel size ($13 \times 24\,km^2$ for OMI, $80 \times 40\,km^2$ for GOME-2) which makes smaller patterns invisible. Satellite data also suffer from instrumental drifts and require validation involving mostly ground-based DOAS instruments (Pinardi et al., 2010), airborne in-situ measurements (Bucsela et al., 2008; Boersma et al., 2008) or more seldom, airborne DOAS instruments (Heue et al., 2005). An aircraft enables covering the spatial extent of a pixel in a short time, but such an experiment is expensive and requires dedicated aircraft.

Ultra-light aircraft are well-suited for NO_2 studies. Their ceiling is relatively low but, at least in polluted zones, most of the NO_2 is close to the surface. Aircraft modifications are much easier than on a normal plane since they do not require certifications from the aeronautics authorities. Ultra-light aircraft have yet been used to study actinic flux (Junkermann, 2001), aerosols profiles (Chazette et al., 2007; Raut and Chazette, 2008), or formaldehyde distribution (Junkermann, 2009).

The Earth Challenge expedition (De Maegd, 2010), which took place in 2009, involved four ultralight aircraft flying from Australia to Belgium. It provided an opportunity to develop and test a new compact DOAS instrument, namely the ULM-DOAS. In comparison with previous airborne DOAS experiments (e.g. Bruns et al., 2006; Prados-Roman et al., 2011; Merlaud et al., 2011), the optical set-up is very simple. We just record the scattered light intensity at the horizon within a large field-of-view without any

AMTD
5, 1947–1984, 2012

telescope or scanner. However, this measurement geometry optimizes the sensitivity to boundary layer NO_2 while it limits the errors due to aircraft attitude instabilities.

In the next section we describe the technical aspects of the ULM-DOAS instrument and the Earth Challenge expedition. The methods used for the data analysis, i.e. the DOAS settings, radiative transfer modeling, and inversion scheme are presented in Sect. 3. In Sect. 4, we study the sensitivity of our measurements to geometrical and geophysical parameters and propagate uncertainties on these parameters in an error budget. The methods and error analysis are applied in Sect. 5 to derive tropospheric NO_2 above interesting areas for which few local measurements have been reported. We compare our measurements with OMI and GOME-2 data for the days where it is possible and we investigate the presence of a soil signature, recently reported in GOME-2 spectra.

2 The ULM-DOAS instrument and the Earth Challenge expedition

2.1 Instrumental description

Figure 2 shows the ULM-DOAS, which was developed at the Belgian Institute for Space Aeronomy (BIRA-IASB) and first used during the Earth Challenge expedition. The light is collected by a 400 µm diameter optical fiber which, during operation, is attached under a wing of the aircraft, pointing forward to the horizon. There is no focusing element at the entrance of the fiber hence the field-of-view is directly related to the numerical aperture of the fiber, which corresponds to 25° (Fig. 1). This choice is motivated in Sect. 4. A black plastic baffle (not shown) is added to limit stray light. The other extremity of the fiber is screwed to the spectrometer which lies inside a $27 \times 27\,cm^2$ aluminium box, together with a PC-104 which controls it. The spectrometer is an AvaSpec-2048 with a 50 µm entrance slit and a $600\,l\,mm^{-1}$ grating, blazed at 300 nm. It covers the spectral range from 200–750 nm at a resolution of approximately 1.2 nm Full Width at

AMTD
5, 1947–1984, 2012

Half Maximum (FWHM) at 460 nm. A GPS antenna is connected to the PC-104 for georeferencing the measurements. The whole set-up is powered by the aircraft's 12V.

While measuring, the instrument records spectra continuously at an integration time of 5 ms. These spectra are averaged on a period of 5 s to reduce the noise. The dark current is estimated from the mean of the signal in the range 280–300 nm, where the atmosphere is opaque due to ozone absorption. Preliminary DOAS analyses (see Sect. 3.1) with preconvoluted cross sections are done in real time and saved on a USB key attached to the aluminium box. This is important to monitor easily the behavior of the instrument, especially when no scientists are present, as was the case during the Earth Challenge expedition.

2.2 The Earth Challenge expedition

Earth Challenge was a 27 000 km expedition between Australia and Belgium, onboard four ultralight aircraft, which took place in April and November 2009 (De Maegd, 2010). The team left from Sydney (Australia) on 5 April 2009 and reached Bangkok (Thailand) on 30 April 2009 in 37 flights. The second phase started from Bangkok after the monsoon time, on 30 October 2009 and ended after 21 flights in Charleroi (Belgium) on 5 December 2009. The objective of the 7 pilots team, besides reaching Belgium, was to draw the public's attention to major environmental problems such as sea rising, pollution and climate change, in cooperation with the World Wildlife Fund (WWF). The project was co-supported by BIRA-IASB which used this opportunity to develop and test the new instrument described in the previous section.

The aircraft used were four Coyote RANS-S6. Their cruise speed is 180 km h^{-1} and they can reach an altitude of 4.8 km, with a payload (including pilots) of 300 kg. The range is around 700 km but additional 50 l oil tanks were added for the longest flights of the expedition, e.g. the 874 km cross of the Oman's Gulf between Gwadar (Pakistan) and Dubai (United Arab Emirates).

Figure 3 shows the second part of the expedition, superimposed on a monthly averaged map of GOME-2 NO_2 tropospheric measurements during November 2009. The

AMTD
5, 1947–1984, 2012

circled numbers correspond to the areas further studied in this work. Except for India and the Po Valley, they correspond to places were few local NO_x measurements have been reported in the literature. For some of them, e.g. megacitities like Karachi and Riyadh, it is expectable to find high pollution levels. During the first part, instrumental problems prevented to make measurements after Brisbane (Australia).

3 Spectral analysis and NO_2 column retrieval

This section describes the three steps of the data analysis: the DOAS fit which retrieves the integrated gas concentration along the photon path, the air mass factor calculation used to derive a geophysical interpretation from the DOAS fit, and finally the propagation of the different uncertainties in the error budget.

3.1 DOAS analysis

Molecular absorption of NO_2 is commonly retrieved in uv-visible atmospheric spectra using the DOAS technique (Platt and Stutz, 2008). This method relies on the fact that, for certain molecules including NO_2, the absorption cross-section varies much more rapidly with wavelength than the scattering effects (Rayleigh and Mie). In practice, a measured spectrum ($I(\lambda)$) is divided by a reference one ($I_{\mathrm{ref}}(\lambda)$) to remove solar Fraunhofer structures and reduce instrumental effects. The slow variations in the logarithm of this ratio are filtered out with a low-order polynomial ($P(\lambda)$) and the remaining absorption structures are fitted in a least-square sense with high-pass filtered laboratory cross-sections ($\sigma_i'(\lambda)$). DOAS enables thus to apply the Beer-Lambert law in the atmosphere, in a form that can be written as:

$$\ln \frac{I(\lambda)}{I_{\mathrm{ref}}(\lambda)} = -\sum_i \sigma_i'(\lambda) \cdot \mathrm{DSCD}_i + P(\lambda). \quad (1)$$

AMTD
5, 1947–1984, 2012

In the above equation the index *i* represents one particular absorber. DOAS analysis results are, for each considered absorber, in the form of differential slant column density (DSCD), i.e. the differences between the concentration integrated along the optical path of the measurement (SCD) and the corresponding quantity in the reference spectrum (SCD_{ref}).

$$DSCD = SCD - SCD_{ref} \quad (2)$$

Table 1 lists the DOAS analysis settings used for the retrievals of NO_2 DSCDs. These settings were implemented in the QDOAS software, developed at BIRA-IASB (Fayt et al., 2011). The Ring effect (Grainger and Ring, 1962) is caused by rotational Raman scattering by O_2 and N_2 and produces a filling-in of solar Fraunhofer lines in scattered light. We fit a Ring pseudo-absorption as described in Chance and Spurr (1997) to take it into account. Additionally, we include an empirical sand cross-section (Richter et al., 2011) above desert areas (see Sect. 5.3).

Figure 4 presents a typical NO_2 DOAS result. The corresponding analyzed and reference spectra originate from the same flight on 2 December 2009 but the former was recorded in the Po Valley while the latter above a clean zone at higher altitude. The first three panels show the simultaneously fitted absorptions of NO_2 (panel a), water vapor (panel b), the $(O_2)_2$ collision complex, referred as O_4 (panel c), and ozone (panel d) in the form of optical densities relative to the reference spectrum. The lowest panel displays the fit residuals. The four absorbers are clearly detected, and NO_2 optical density is particularly high (1 % peak-to-peak) which is expectable in the Po Valley, one of the most polluted areas in Europe regarding NO_2 (see Fig. 3)

3.2 Air mass factor calculation

The DOAS analysis per se provides only a qualitative insight into the NO_2 field. Indeed, beside being relative to a reference column, a DSCD depends on the light path through the atmosphere. A more relevant geophysical quantity is the NO_2 concentration integrated vertically through the atmosphere, i.e. the NO_2 vertical column density (VCD).

AMTD
5, 1947–1984, 2012

The air mass factor (AMF) is defined as the ratio between the slant and vertical column densities

$$\mathrm{AMF} = \mathrm{SCD}/\mathrm{VCD}. \quad (3)$$

In the following, we describe our assumptions to derive the tropospheric VCD from Eq. (3), and the practical calculations of a tropospheric AMF.

3.2.1 Assumptions for the tropospheric column retrieval

As we are interested in the tropospheric vertical column, we split the slant column density in its tropospheric and stratospheric components:

$$\mathrm{SCD} = \mathrm{AMF}_{\mathrm{tropo}} \cdot \mathrm{VCD}_{\mathrm{tropo}} + \mathrm{AMF}_{\mathrm{strato}} \cdot \mathrm{VCD}_{\mathrm{strato}}. \quad (4)$$

Using the above expression for the slant column density in Eq. (2) leads to the following formula for the measured DSCD:

$$\mathrm{DSCD} = \mathrm{AMF}_{\mathrm{tropo}} \cdot \mathrm{VCD}_{\mathrm{ropo}} + \mathrm{AMF}_{\mathrm{strato}} \cdot \mathrm{VCD}_{\mathrm{strato}} - \left(\mathrm{AMF}_{\mathrm{tropo}_{\mathrm{ref}}} \cdot \mathrm{VCD}_{\mathrm{tropo}_{\mathrm{ref}}} + \mathrm{AMF}_{\mathrm{strato}_{\mathrm{ref}}} \cdot \mathrm{VCD}_{\mathrm{strato}_{\mathrm{ref}}}\right). \quad (5)$$

Equation (5) may be simplified if the reference spectrum is well chosen. Due to its short lifetime in the troposphere, $\mathrm{VCD}_{\mathrm{tropo}_{\mathrm{ref}}}$ column can be assumed to be null far enough from the NO_2 emission sources, e.g. above the deserts or the oceans. If on the other hand the reference spectrum is taken the same day when the sun is high enough, stratospheric contributions cancel each other since the stratospheric NO_2 is slowly varying during the day and the stratospheric AMF is constant. Equation (5) can thus be approximated as:

$$\mathrm{DSCD} = \mathrm{AMF}_{\mathrm{tropo}} \cdot \mathrm{VCD}_{\mathrm{tropo}}. \quad (6)$$

From Eq. (6) it is possible to retrieve $\mathrm{VCD}_{\mathrm{tropo}}$ assuming independence between a given $\mathrm{AMF}_{\mathrm{tropo}}$ and $\mathrm{VCD}_{\mathrm{tropo}}$. This is usually done and implies that the NO_2 loading

AMTD
5, 1947–1984, 2012

is optically thin enough that it does not influence the radiative transfer. The resulting AMF still depends then on the NO_2 profile but not on its absolute value. We use this hypotheses but check its validity in the next section where we detail the practical AMF_{tropo} calculation.

3.2.2 Radiative transfer and assumptions on NO_2 and aerosol extinction profiles

The radiative transfer model used in this study is UVspec/DISORT (Mayer and Kylling, 2005). It is based on the discrete ordinate method and deals with multiple scattering in a pseudo-spherical approximation. Given the wavelength, the observation's geometry relative to the Sun and the atmospheric state, the model calculates the scattered radiance and the absolute slant column density (SCD) of molecular absorbers. It is thus possible to derive AMF_{tropo} from Eq. (3). By limiting the altitude grid to a 10 km maximum, we neglect the stratospheric contribution as discussed in the previous paragraph.

Considering the DOAS fitting window (see Sect. 3.1), calculations are done at 460 nm. The GPS data recorded along with the spectra enabled to calculate the Sun's position and the aircraft's heading accurately. To take into account the numerical aperture of the optical fiber, each SCD is the weighted mean of 13 SCDs at uniformly distributed angles between −12 and 12° around the horizon. The weights correspond to the different radiances calculated in the respective intermediate SCD geometries.

The NO_2 and aerosol profiles in the model both correspond to a well-mixed boundary layer and negligible concentrations and extinction in the free troposphere (for NO_2, see Fig. 5). The boundary layer heights are interpolated from ECMWF (European Centre for Medium-Range Weather Forecasts) forecasts at the times and heights of the measurements, except for Riyadh (see Sect. 5.1). In clean areas, these assumptions may not be realistic enough, as we showed in a previous airborne experiment in Arctic (Merlaud et al., 2011). But the measurements presented in this study were recorded in polluted zone where aerosols and $NO_2$are dominant close to the surface. Considering

AMTD
5, 1947–1984, 2012

NO_2, Heland et al. (2002) studied the effect of the profile's shape comparing aircraft in-situ and OMI data, he concluded it was relatively weak. Boersma et al. (2009) also assumed a homogeneous boundary layer to compare in-situ surface NO_2 concentrations with SCIAMACHY and OMI columns. This is also confirmed by the few tropospheric NO_2 lidar measurements available (Volten et al., 2009). Considering aerosol extinction, the many lidar profiles available in polluted zones (e.g. Landulfo et al., 2003; Guibert et al., 2005) indicate a maximum extinction in the boundary layer, even if the shape is less step-like. In practice, we derive aerosol optical thickness at 550 nm from MODIS (retrieved from Giovanni, Acker and Leptoukh, 2007) and divide it by the BLH to get the extinction coefficient. We then scale this extinction coefficient at 460 nm using the Angstrom coefficient as described in Nebuloni (2005), and derive visibility at this wavelength from the Koshmieder law (Koshmieder, 1926). The same approach to estimate the visibility will be used for the GEOS-R satellite (NOAA-NESDIS, 2010).

Figure 5 shows the variation of the AMF with the observation's altitude for the idealized profile considered in the model. In the calculations, the solar zenith angle was 45°, the visibility 20 km, and the albedo 0.1. These numbers are representative of the conditions of the campaign. The AMF and thus the sensitivity are maximum when the aircraft flies at 500 m altitude, where the AMF is around 5.2. The AMF then decreases sharply when the plane crosses the boundary layer. This indicates that this parameter is important for the accuracy of our measurements.

For the retrievals, air mass factors are interpolated in look-up tables calculated for each flight around the places of interest (see Fig. 3). The look-up tables parameters are aircraft's altitude, relative azimuth, boundary layer height, visibility, albedo, solar zenith angle. For a given flight, the first two parameters vary according to the GPS data, while the last four are set constant.

AMTD
5, 1947–1984, 2012

4 Sensitivity studies and error analysis

Figure 6 shows the variation of air mass factor for the visibility, pitch angle and albedo in the typical ranges of the flights. Surface visibility plays the largest role in the AMF variation, which is understandable from the limb-geometry of our measurements. For the same reason, albedo very weakly affects the air mass factor. Indeed, most of the detected photons are scattered before the ground, as illustrated in Fig. 1, and thus not affected by its reflectivity. This is very different from nadir-looking satellites, for which the albedo uncertainty matters much more in the final error budget, as can be seen in Boersma et al. (2004). Finally, the small effect of the pitch angle is due to the large field-of-view: the multiple line-of-sights smooths the variation in aircraft attitude.

Figure 7 displays an effect which is often neglected in DOAS studies, i.e. the influence of the studied absorber on the radiative transfer and thus the AMF itself. When the absorber's column, in our case, NO_2, is high enough, it can not be considered as optically thin and reduces the air mass factor. The effect is visible from 6×10^{16} molec cm^{-2}, corresponding to an optical density of 0.02. We believe this error should be considered when accurate errors budgets are necessary since it could play a larger role than the cross-section uncertainties for instance, which are often taken into account. In particular, low-elevation MAX-DOAS measurements in polluted regions are likely to be affected by this error.

Table 2 indicates the uncertainties considered in this study and their effect on the relative air mass factor. The accuracy of the ECMWF boundary layer heights was investigated by Palm et al. (2005), who concluded that the BLH were 200–400 m underestimated. We thus consider an error of 300 m for this parameter. This is the major source of error in our measurements, leading to 15 % uncertainty on the AMF. Considering the albedo, Kleipool et al. (2008) derived an absolute uncertainty of 0.01 to 0.02 for the OMI albedo used in our AMF calculation. We use 0.05 as this parameter's role is not critical anyway (1 % on AMF). The uncertainty in the visibility is set to 6 km. This value originates from the propagation in Koshmieder's law of the 300 m uncertainty for

AMTD
5, 1947–1984, 2012

the BLH already mentionned and a typical uncertainty of 0.1 for the AOT which we derive from a comparison between Modis Aqua and Calipso (Kittaka et al., 2011). Finally, the error due to the effect of NO_2 on the radiative transfer leads to 1 % uncertainty on the AMF, a small effect, but comparable to the errors due to the pitch and the albedo.

In practice, the error on the tropospheric column is derived from Eq. (6) as:

$$\sigma_{\mathrm{VCD}_{\mathrm{tropo}}} = \sqrt{\left(\frac{\sigma_{\mathrm{DSCD}}}{\mathrm{AMF}}\right)^2 + \sigma_{\mathrm{AMF}}^2 \left(\frac{\mathrm{DSCD}}{\mathrm{AMF}^2}\right)^2}. \quad (7)$$

In this equation, the error on the DSCD(σ_{DSCD}) is an output of the DOAS analysis (Fayt et al., 2011). The error on the AMF is the quadratic sum of the different errors discussed previously. Note that we take into account the correlation between the boundary layer height and the visibility introducing an adequate term in Table 2. The correlation coefficient is estimated from the values of the BLH and visibility in Table 3.

5 Results

This section presents the results for the flights of Fig. 3. We first compare our measurements with satellite data (OMI and GOME-2) for the flights when these are available at the location of our flights, and indicate the NO_2 loading above other interesting hot spots. Then, we demonstrate that our measurements are suitable to estimate a flux for isolated point source like Riyadh. Finally, we confirm a soil signature in the spectra that closely matches results from a previous study on satellite data (Richter et al., 2011).

5.1 Comparisons with satellites

Figures 8, 9, and 10 compare OMI and GOME-2 data with our ULM-DOAS measurements, respectively above Rajasthan (15 November 2009), Po Valley (2 December 2009), and Saudi Arabia (24 November 2009). The flight conditions are detailed respectively in line 2, 6, and 4 of Table 3 . These three areas represent an interesting

AMTD
5, 1947–1984, 2012

sample of the global tropospheric NO_2 field above land. Indeed, the two first ones indicate rather homogeneous tropospheric NO_2 loadings, but absolute values are one order of magnitude higher in the Po Valley than in Rajasthan. In Saudi Arabia, the situation is very different, since one megacity, Riyadh, is surrounded by desert with very few NO_2 sources. This yields high columns close to the city, rapidly decreasing to reach neglectable values further away above the desert.

The agreement between ULMDOAS and satellite data is qualitatively good for the three days, but better quantitatively above Rajasthan and Italy than above Saudi Arabia. Above Rajasthan (Fig. 8), the tropospheric NO_2 columns seen from the aircraft spans from 0.1 ± 0.1 to $2.8 \pm 1 \times 10^{15}$ molec cm^{-2}, whereas from OMI 0.5 ± 0.6 to $1.7 \pm 1 \times 10^{15}$ molec cm^{-2}. This discrepancy might be explained by a dilution effect, indeed OMI is not able to resolve spatial structures at scales smaller than 20 km. Most of the points are however inside the error bars. Considering the Po Valley (Fig. 9), OMI data are unfortunately affected by the row anomaly (Boersma et al., 2011) but the GOME-2 measurement is very close to our airborne measurements. The NO_2 column in the Po Valley appears constant around $2.5 \pm 0.5 \times 10^{16}$ molec cm^{-2}.

Figure 10 indicates a positive bias between ULMDOAS measurements and satellite data in the region where the NO_2 columns are highest. In the case of GOME-2, this can be explained by the dilution effect considering the size of the pixels, and partly by the 3 h time difference. Considering OMI data, these effects are expected to be much smaller since the two measurements are almost simultaneous and the spatial resolution of OMI is much better than GOME-2. For this area, standard MODIS Aqua data are not available and we had to use the MODIS Deep blue product AOT, i.e. 0.2, to estimate the visibility. There is an Aeronet station close to Riyadh (Sabbah and Hasan, 2008) but the data sets is discontinuous for the period of the flight, and the only AOT measurement point, 0.45, leads to a reduced AMF and thus an even higher bias between our measurements and OMI. Note that an offset could also originate from an error in the boundary layer height, which is close to the observation altitude (see Table 3). For this area only, we use the GDAS archived boundary layer height instead of

AMTD
5, 1947–1984, 2012

the ECMWF which is surprisingly low for this day and leads to even larger discrepancies between OMI data and our measurements. This persistent bias and the facts that no validation has been achieved to our knowledge in desertic areas leads us to point out the necessity of other measurements to check for a possible underestimation of OMI data in similar areas.

Figure 11 helps to interpret the patterns seen in the pink box of Fig. 10. It presents the OMI pixels around Riyadh superimposed on a map with Riyadh extent, the main wind direction retrieved from GDAS and the ULMDOAS flight track. The color code is the same for OMI and ULMDOAS data. The megacity occupies an area slightly smaller than three OMI pixels, and the aircraft was flying 70 km North-West of it when it detected the highest NO_2 columns. ULMDOAS and OMI data are both understandable from the wind direction as a pollution plume of the city, which would have, compared to this source, a relatively similar horizontal extent. It is thus possible to calculate the NO_2 flux, integrating horizontally the column and then multiplying by the projection of the wind vector on the normal to the flight track. Such a calculation leads to a flux of $153\,\mathrm{mol\,s^{-1}}$. Note that to obtain this value we added the ghost part of the plume West of 46.7° E depicted in green in Fig. 10. Due to that and the wind uncertainties, we find it difficult to estimate the associated error. Nethertheless, the value is relatively close to the one derived by Beirle et al. (2011) from satellite, i.e. $187 \pm 14\,\mathrm{mol\,s^{-1}}$. This points out that, providing accurate wind data, our instrument would be useful to estimate flux from megacities. This has been done from cars (e.g. Johansson et al., 2009) but an aircraft covers an exhaust plume in a much shorter time and is thus less sensitive to temporal variations of the NO_2 field.

5.2 Other interesting measurements

Table 3 summarizes the main results of the campaign and their measurements'conditions. The numbers representing the measurements are related to Fig. 3. Note that the mass concentration in the last column is only indicative. We do not estimate its uncertainty, which would be correlated to the uncertainty on the boundary

AMTD
5, 1947–1984, 2012

layer height, because even if our measurements have a finer spatial resolution than satellites, the real NO_2 field can be much more heterogeneous than seen by our instrument. These consideration also apply to our measured vertical columns but they are less relevant in the context of comparing with satellite data.

Beside the measurements described in the previous section, we report the measured NO_2 tropospheric column close to three large cities, Chittagong (1), Karachi (3) and Benghazi (5). The latter two are usually visible from OMI and for both of them corresponding Modis Aqua AOT are available. Karachi is the largest city in the world regarding population (15 millions inhabitants). We estimate at $3.2 \pm 1 \times 10^{16}$ molec cm^{-2} the tropospheric NO_2 column during the landing on an airport 15 km east from the city center. Benghazi is comparatively a much smaller city. Nethertheless we detected there the highest NO_2 loading of the campaign, $5.7 \pm 2 \times 10^{16}$ molec cm^{-2}. Such high columns are certainly linked to the industries of the city and particularly to its refineries.

Figure 12 is a picture taken by the pilots during the campaign, while flying above Chittagong. It shows a major industry of the city, i.e. one of the largest ship cemeteries in the world. The picture is simultaneous to high measured slant columns, around 4×10^{16} molec cm^{-2}. However, we did not convert these values to vertical columns since no AOT data was available for the day of the flight. It is however obvious from the picture that the visibility is quite small, probably under 5 km. This may result from a combination of a heat fog and of aerosols from the city. We can expect thus the AMF to be very small, which suggests that the NO_2 pollution was probably very high in this region.

5.3 Soil signature above desert

Richter et al. (2011), while improving GOME-2 NO_2 retrieval, derived empirically a soil signature, visible in the spectra corresponding to desertic areas. The inclusion of this signature yielded an improvement in the DOAS fit, mostly visible in regions with bare soils, e.g. Sahara and Arabic Peninsula. Richter et al. (2011) also found a similar spectral shape in a lab experiment using sand. They nethertheless pointed out that

AMTD
5, 1947–1984, 2012

more measurements were necessary to firmly confirm the attribution to a soil effect, particularly due to possible correlations with O_4.

Figure 13 shows the fit of the soil signature (Richter et al., 2011) together with O_4, in a spectrum recorded above Saudi Arabia, on 24 November 2009. DOAS settings, except the fitting window, are given in Table 1. The reference spectrum was recorded in Italy on 2 December 2009, which leads to a larger signal of the soil signature than using a reference spectrum from Saudi Arabia. This is understandable if the signature really originates from bare soil, which are present all along the flight on 24 November 2009, and thus in all the spectra, but not in Italy.

Figure 14 displays the time series of the DOAS fit results for the soil signature (upper panel) and the RMS fit, including or not the soil signature (lower panel). Several episodes of enhanced soil signal are visible, the largest one just before 11:30 UT. On the lower panel we see that these episodes appear as increased RMS time series if the DOAS fit does not include the soil signature (green curve). If the soil signature is taken into account (blue curve), the RMS is relatively constant over the flight.

The episodes just discussed are simultaneous to a sand storm that was reported by the pilots while approaching Medina. This reinforces our confidence that the soil signature identified by Richter et al. (2011) has indeed a geophysical origin, and that it can be detected on suspended sand particles.

6 Conclusions

We presented a new airborne instrument designed for tropospheric NO_2 column measurement, the ULM-DOAS. It was operated during the Earth Challenge expedition which took place in 2009 between Australia and Belgium. The ULMDOAS was designed to fit onboard the ultralight aircraft of the expedition and to be fully automatic. The set-up is simple without any attitude stabilization, but related uncertainties are minimized by using a large field-of-view. The limb geometry of the instrument makes it suitable for low-flying aircraft and maximizes the sensitivity to boundary layer NO_2.

AMTD
5, 1947–1984, 2012

Measurements during the Earth Challenge expedition are consistent with OMI and GOME-2 data and interesting on their own since very few validation campaigns were performed in the countries overflown. Highest NO_2 loadings were detected above megacities like Karachi ($3.2 \pm 1 \times 10^{16}$ molec cm^{-2}) or Benghazi ($5.7 \pm 2 \times 10^{16}$ molec cm^{-2}). Our measurements also confirm the recent finding of a soil signature above desert.

Compared to satellite data, our instrument is able to detect higher spatial frequency patterns in the NO_2 field (around 5 km when an OMI pixel width is 13 km). We believe it is well-suited for tropospheric NO_2 column validation, offering a low-cost alternative to larger aircraft measurements. Such measurements are also well-suited for flux measurements from extended sources, providing accurate wind data. A useful improvement would be the addition of a compact PTU sensor, which would indicate the aircraft position relative to the boundary layer, which we consider to be the major source of uncertainty in our measured tropospheric NO_2 column.

Acknowledgements. This work was supported by the Belgian Ministry of Scientific research. We are grateful to Tom Egerickx, Marc Nevens, and Geert Hemerijckx from our mechanical workshop and to the Earth Challenge team and particularly Michel de Maegd. We also thank Andreas Richter for providing his sand spectral signature, and François Hendrick and Gaia Pinardi for useful discussions.

References

Acker, J. G. and Leptoukh, G.: Online analysis enhances use of NASA Earth science data, Eos Trans. AGU, 88, 2, doi:10.1029/2007EO020003, 2007. 1956

Beirle, S., Boersma, K. F., Platt, U., Lawrence, M. G., and Wagner, T.: Megacity Emissions and Lifetimes of Nitrogen Oxides Probed from Space, Science, 333, 1737–1739, doi:10.1126/science.1207824, 2011. 1960

AMTD
5, 1947–1984, 2012

Boersma, K., Jacob, D., Bucsela, E., Perring, A., Dirksen, R., van der A, R., Yantosca, R., Park, R., Wenig, M., Bertram, T., and Cohen, R.: Validation of OMI tropospheric NO_2 observations during INTEX-B and application to constrain NO_x emissions over the eastern United States and Mexico, Atmos. Environ., 42, 4480–4497, doi:10.1016/j.atmosenv.2008.02.004, 2008. 1949

Boersma, K. F., Eskes, H. J., and Brinksma, E. J.: Error analysis for tropospheric NO_2 retrieval from space, J. Geophys. Res., 109, D04311, doi:10.1029/2003JD003962, 2004. 1957

Boersma, K. F., Jacob, D. J., Trainic, M., Rudich, Y., DeSmedt, I., Dirksen, R., and Eskes, H. J.: Validation of urban NO_2 concentrations and their diurnal and seasonal variations observed from the SCIAMACHY and OMI sensors using in situ surface measurements in Israeli cities, Atmos. Chem. Phys., 9, 3867–3879, doi:10.5194/acp-9-3867-2009, 2009. 1956

Boersma, K. F., Eskes, H. J., Dirksen, R. J., van der A, R. J., Veefkind, J. P., Stammes, P., Huijnen, V., Kleipool, Q. L., Sneep, M., Claas, J., Leitão, J., Richter, A., Zhou, Y., and Brunner, D.: An improved tropospheric NO_2 column retrieval algorithm for the Ozone Monitoring Instrument, Atmos. Meas. Tech., 4, 1905–1928, doi:10.5194/amt-4-1905-2011, 2011. 1959

Bruns, M., Buehler, S. A., Burrows, J. P., Richter, A., Rozanov, A., Wang, P., Heue, K. P., Platt, U., Pundt, I., and Wagner, T.: NO_2 Profile retrieval using airborne multi axis UV-visible skylight absorption measurements over central Europe, Atmos. Chem. Phys., 6, 3049–3058, doi:10.5194/acp-6-3049-2006, 2006. 1949

Bucsela, E. J., Perring, A. E., Cohen, R. C., Boersma, K. F., Celarier, E. A., Gleason, J. F., Wenig, M. O., Bertram, T. H., Wooldridge, P. J., Dirksen, R., and Veefkind, J. P.: Comparison of tropospheric NO_2 from in situ aircraft measurements with near-real-time and standard product data from OMI, J. Geophys. Res., 113, D16S31, doi:10.1029/2007JD008838, 2008. 1949

Chance, K. V. and Spurr, R. J. D.: Ring effect studies: Rayleigh scattering, including molecular parameters for rotational Raman scattering, and the Fraunhofer spectrum, Appl. Optics, 36, 5224–5230, doi:10.1364/AO.36.005224, 1997. 1953, 1968

Chazette, P., Sanak, J., and Dulac, F.: New Approach for Aerosol Profiling with a Lidar Onboard an Ultralight Aircraft: Application to the African Monsoon Multidisciplinary Analysis, Environ. Sci. Technol., 41, 8335–8341, doi:10.1021/es070343y, 2007. 1949

De Maegd, M.: Earth challenge: Sydney-Bruxelles en ULM, La Renaissance du Livre, 2010. 1949, 1951

AMTD
5, 1947–1984, 2012

Fayt, C., De Smedt, I., Letocart, V., Merlaud, A., Pinardi, G., and Van Roozendael, M.: QDOAS, Software User Manual, Belgian Insitute for Space Aeronomy, Brussels, Belgium, 2011. 1953, 1958

Grainger, J. F. and Ring, J.: Anomalous Fraunhofer Line Profiles, Nature, 193, doi:10.1038/193762a0, 1962. 1953

Guibert, S., Matthias, V., Schulz, M., Bosenberg, J., Eixmann, R., Mattis, I., Pappalardo, G., Ritaperrone, M., Spinelli, N., and Vaughan, G.: The vertical distribution of aerosol over Europesynthesis of one year of EARLINET aerosol lidar measurements and aerosol transport modeling with LMDzT-INCA, Atmos. Environ., 39, 2933–2943, doi:10.1016/j.atmosenv.2004.12.046, 2005. 1956

Harder, J. W. and Brault, J. W.: Atmospheric measurements of water vapor in the 442-nm region, J. Geophys. Res., 102, 6245–6252, doi:10.1029/96JD01730, 1997. 1968

Heland, J., Schlager, H., Richter, A., and Burrows, J. P.: First comparison of tropospheric NO_2 column densities retrieved from GOME measurements and in situ aircraft profile measurements, Geophys. Res. Lett., 29, 1983, doi:10.1029/2002GL015528, 2002. 1956

Heue, K.-P., Richter, A., Bruns, M., Burrows, J. P., v. Friedeburg, C., Platt, U., Pundt, I., Wang, P., and Wagner, T.: Validation of SCIAMACHY tropospheric NO_2-columns with AMAXDOAS measurements, Atmos. Chem. Phys., 5, 1039–1051, doi:10.5194/acp-5-1039-2005, 2005. 1949

Jacob, D.: Introduction to Atmospheric Chemistry, illustrated edition edn., Princeton University Press, 1999. 1948

Johansson, M., Rivera, C., de Foy, B., Lei, W., Song, J., Zhang, Y., Galle, B., and Molina, L.: Mobile mini-DOAS measurement of the outflow of NO_2 and HCHO from Mexico City, Atmos. Chem. Phys., 9, 5647–5653, doi:10.5194/acp-9-5647-2009, 2009. 1960

Junkermann, W.: An Ultralight Aircraft as Platform for Research in the Lower Troposphere: System Performance and First Results from Radiation Transfer Studies in Stratiform Aerosol Layers and Broken Cloud Conditions, J. Atmos. Ocean. Tech., 18, 934, doi:10.1175/1520-0426(2001)018<0934:AUAAPF>2.0.CO;2, 2001. 1949

Junkermann, W.: On the distribution of formaldehyde in the western Po-Valley, Italy, during FORMAT 2002/2003, Atmos. Chem. Phys., 9, 9187–9196, doi:10.5194/acp-9-9187-2009, 2009. 1949

AMTD
5, 1947–1984, 2012

Kittaka, C., Winker, D. M., Vaughan, M. A., Omar, A., and Remer, L. A.: Intercomparison of column aerosol optical depths from CALIPSO and MODIS-Aqua, Atmos. Meas. Tech., 4, 131–141, doi:10.5194/amt-4-131-2011, 2011. 1958

Kleipool, Q. L., Dobber, M. R., de Haan, J. F., and Levelt, P. F.: Earth surface reflectance climatology from 3 years of OMI data, J. Geophys. Res., 113, D18308, doi:10.1029/2008JD010290, 2008. 1957

Koshmieder, H.: Theorie der horizontale Sichtweite, Beitrag. Atm. Physik., 12, 33–55, 1926. 1956

Landulfo, E., Papayannis, A., Artaxo, P., Castanho, A. D. A., de Freitas, A. Z., Souza, R. F., Vieira Junior, N. D., Jorge, M. P. M. P., Sánchez-Ccoyllo, O. R., and Moreira, D. S.: Synergetic measurements of aerosols over São Paulo, Brazil using LIDAR, sunphotometer and satellite data during the dry season, Atmos. Chem. Phys., 3, 1523–1539, doi:10.5194/acp-3-1523-2003, 2003. 1956

Levelt, P., van den Oord, G., Dobber, M., Malkki, A., Visser, H., de Vries, J., Stammes, P., Lundell, J., and Saari, H.: The ozone monitoring instrument, IEEE T. Geosci. Remote., 44, 1093–1101, doi:10.1109/TGRS.2006.872333, 2006. 1949

Mayer, B. and Kylling, A.: Technical note: The libRadtran software package for radiative transfer calculations – description and examples of use, Atmos. Chem. Phys., 5, 1855–1877, doi:10.5194/acp-5-1855-2005, 2005. 1955

Merlaud, A., Van Roozendael, M., Theys, N., Fayt, C., Hermans, C., Quennehen, B., Schwarzenboeck, A., Ancellet, G., Pommier, M., Pelon, J., Burkhart, J., Stohl, A., and De Mazière, M.: Airborne DOAS measurements in Arctic: vertical distributions of aerosol extinction coefficient and NO2 concentration, Atmos. Chem. Phys., 11, 9219–9236, doi:10.5194/acp-11-9219-2011, 2011. 1949, 1955

Munro, R., Eisenger, M., Anderson, C., Callies, J., Carpaccioli, E., Lang, R., Lefevre, A., Livschitz, Y., and Albinana, A.: GOME-2 on MetOp, in: The 2006 EUMETSAT Meteorological Satellite Conference, 2006. 1949

Nebuloni, R.: Empirical relationships between extinction coefficient and visibility in fog, Appl. Optics, 44, 3795–3804, doi:10.1364/AO.44.003795, 2005. 1956

NOAA-NESDIS: Algorithm Theoretical Basis Document For Visibility, Tech. rep., Center for satellite applications and research, 2010. 1956

AMTD
5, 1947–1984, 2012

Palm, S. P., Benedetti, A., and Spinhirne, J.: Validation of ECMWF global forecast model parameters using GLAS atmospheric channel measurements, Geophys. Res. Lett., 32, L22S09, doi:10.1029/2005GL023535, 2005. 1957

Pinardi, G., Lambert, J., Granville, J., Roozendael, M. V., Delcloo, A., Backer, H. D., Valks, P., and Hao, N.: Overview of the validation of GOME-2 total and tropospheric NO_2 columns, in: EUMETSAT meteorological satellite conference, 2010. 1949

Platt, U. and Stutz, J.: Differential Optical Absorption Spectroscopy: Principles and Applications, Physics of Earth and Space Environments, Springer, Berlin, 2008. 1949, 1952

Prados-Roman, C., Butz, A., Deutschmann, T., Dorf, M., Kritten, L., Minikin, A., Platt, U., Schlager, H., Sihler, H., Theys, N., Van Roozendael, M., Wagner, T., and Pfeilsticker, K.: Airborne DOAS limb measurements of tropospheric trace gas profiles: case studies on the profile retrieval of O_4 and BrO, Atmos. Meas. Tech., 4, 1241–1260, doi:10.5194/amt-4-1241-2011, 2011. 1949

Raut, J.-C. and Chazette, P.: Radiative budget in the presence of multi-layered aerosol structures in the framework of AMMA SOP-0, Atmos. Chem. Phys., 8, 6839–6864, doi:10.5194/acp-8-6839-2008, 2008. 1949

Richter, A., Begoin, M., Hilboll, A., and Burrows, J. P.: An improved NO_2 retrieval for the GOME-2 satellite instrument, Atmos. Meas. Tech., 4, 1147–1159, doi:10.5194/amt-4-1147-2011, 2011. 1953, 1958, 1961, 1962

Sabbah, I. and Hasan, F. M.: Remote sensing of aerosols over the Solar Village, Saudi Arabia, Atmos. Res., 90, 170–179, doi:10.1016/j.atmosres.2008.02.004, 2008. 1959

Vandaele, A.: Measurements of the NO2 absorption cross-section from 42 000 cm^{-1} to 10 000 cm^{-1} (238-1000 nm) at 220 K and 294 K, J. Quant. Spectrosc. Ra., 59, 171–184, doi:10.1016/S0022-4073(97)00168-4, 1998. 1968

Volten, H., Brinksma, E. J., Berkhout, A. J. C., Hains, J., Apituley, J. B., Bergwerff, G. R. V. d. H., A., Dirksen, R. J., Calabretta-Jongen, S., and Swart, D. P. J.: NO_2 lidar profile measurements for satellite interpretation and validation, J. Geophys. Res., 114, D24301, doi:10.1029/2009JD012441, 2009. 1956

WHO: Health aspects of air pollution with particulate matter, ozone, and nitrogen dioxide, Report on a WHO working group, World Health Organization, 2003. 1949

AMTD
5, 1947–1984, 2012

Table 1. DOAS analysis settings.

Fitting window	431–495 nm
NO_2	Vandaele (1998)
O_4	Hermans http://www.aeronomie.be/spectrolab/o2.htm
H_2O	Harder and Brault (1997)
Ring	Chance and Spurr (1997)
Polynomial order	3

AMTD
5, 1947–1984, 2012

Table 2. Error contributions to the air mass factor (AMF).

	Δ parameters	$\frac{\Delta AMF}{AMF}$
Boundary layer height	300 m	15 %
Visibility	6 km	12 %
Correlation between BLH and visibility	0.95	14 %
Pitch	2°	2 %
SCD	5e16	1 %
Albedo	0.05	1 %

AMTD
5, 1947–1984, 2012

Table 3. Conditions and results of the campaign. See Fig. 3 for the place and date of the measurements. We give the main parameters to calculate the air mass factor (AMF), i.e.: the surface visibility (Vis.), the boundary layer height (BLH), the albedo (Alb.) and the altitude of the aircraft (Alt.). The tropospheric column (Max. VCD_{tropo}) is the maximum found while overflying the areas. The mass concentration is only indicative.

Place and date	Vis. (km)	BLH (km)	Alb.	Alt. (m)	AMF	Max. VCD_{tropo} (molec cm^{-2})	Conc. ($\mu g\, m^{-3}$)
1	?	1.3	0.06	300	?	?	?
2	24	2.1	0.1	600	3.5	$3.4 \pm 1 \times 10^{15}$	1
3	20	1.6	0.11	150	3.5	$3.2 \pm 1 \times 10^{16}$	15
4	15	1.1	0.14	1250	2	$4.4 \pm 1.5 \times 10^{16}$	40
5	23	1.5	0.08	500	5	$5.7 \pm 2 \times 10^{16}$	30
6	10	0.4	0.06	650	2	$3.2 \pm 2 \times 10^{16}$	40

AMTD
5, 1947–1984, 2012

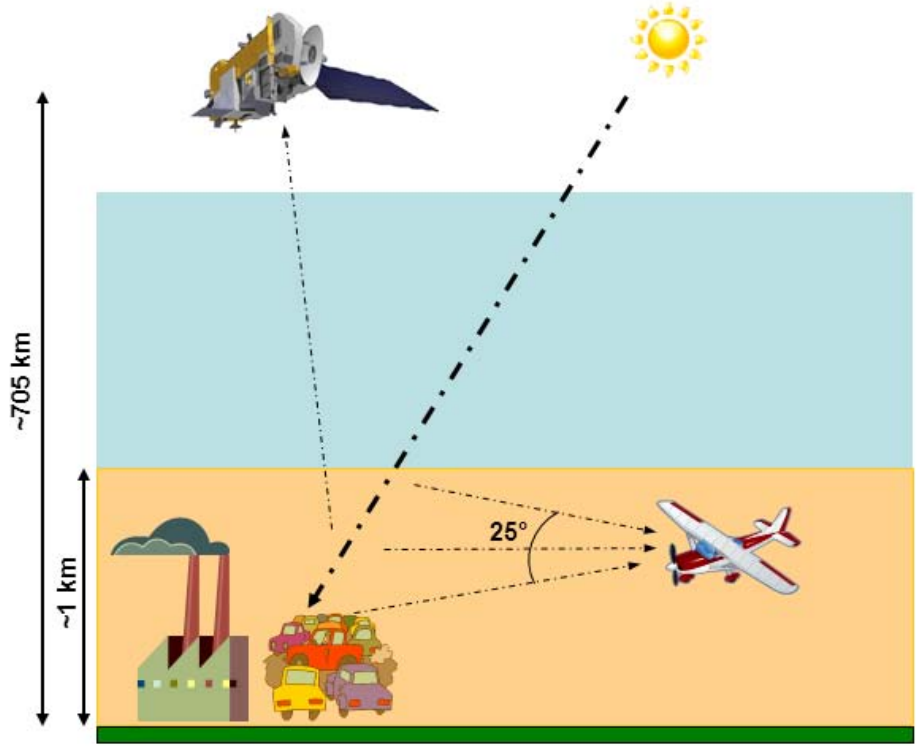

Fig. 1. Geometry of our ULM-DOAS measurements compared to a nadir-looking satellite instrument like OMI.

AMTD
5, 1947–1984, 2012

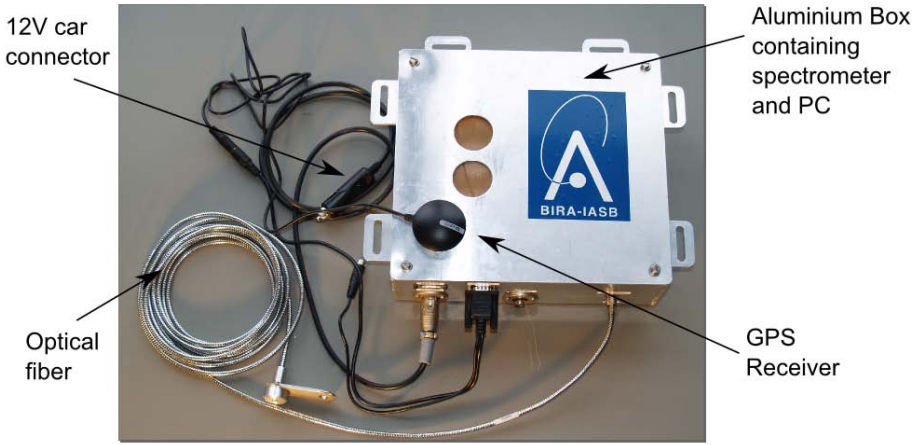

Fig. 2. The ULMDOAS instrument. Inside the box are a compact uv-vis spectrometer and a PC-104. Light is collected directly by the optical fiber and a GPS is used to geolocalize the measurements. The whole system is powered with 12v.

AMTD
5, 1947–1984, 2012

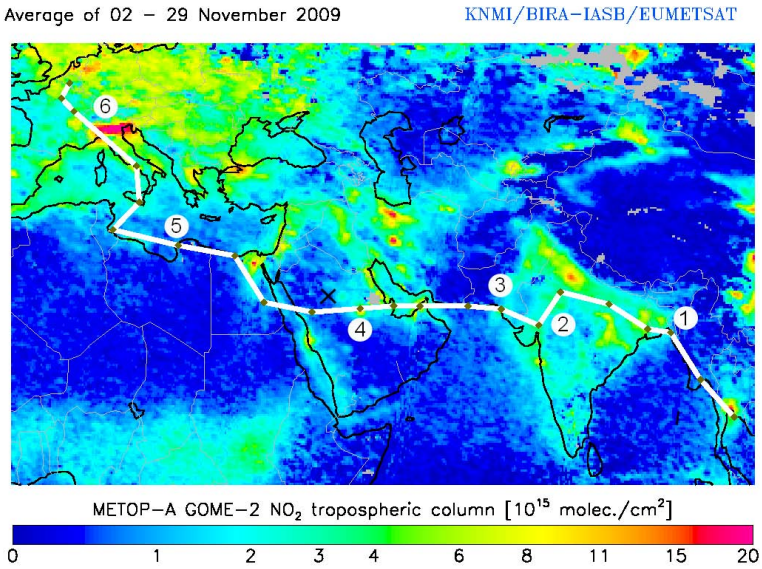

Fig. 3. Flight tracks of the Earth Challenge expedition on a NO2 GOME-2 Map. The numbers correspond to the measurements presented in this paper: (1) Chittagong (Bengladesh, 4 November 2009), (2) Rajasthan (India, 15 November 2009), (3) Karachi (Pakistan, 16 November 2009), (4) Riyadh (Saudi Arabia, 24 November 2009), (5) Benghazi (Libya, 27 November 2009), (6) Po Valley (Italy, 2 December 2009). The cross West of Riyadh indicates a sand storm (see Sect. 5.3).

AMTD
5, 1947–1984, 2012

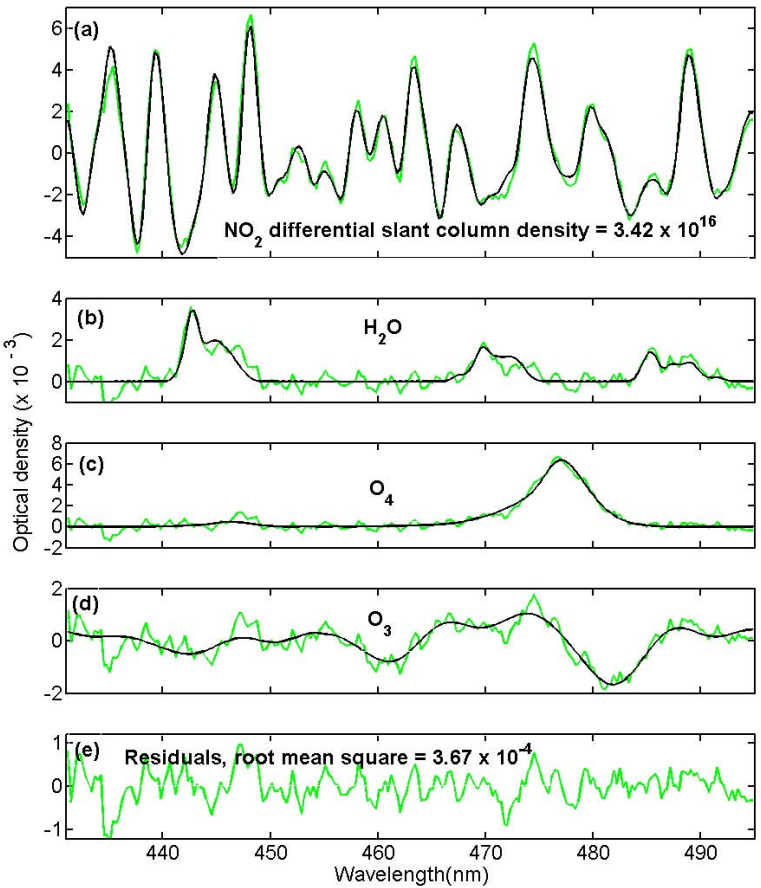

Fig. 4. Example of a DOAS fit, the spectrum was recorded in the Po Valley. Black lines correspond to molecular cross-sections scaled to the detected absorptions in the measured spectrum (green lines).

AMTD
5, 1947–1984, 2012

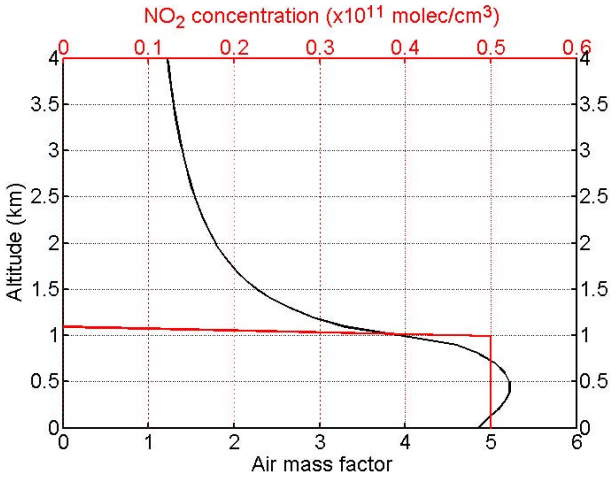

Fig. 5. Air mass factor versus altitude (black) for an idealized NO_2 tropospheric profile (red) well-mixed in the boundary layer and of negligible concentration in the free troposphere.

AMTD
5, 1947–1984, 2012

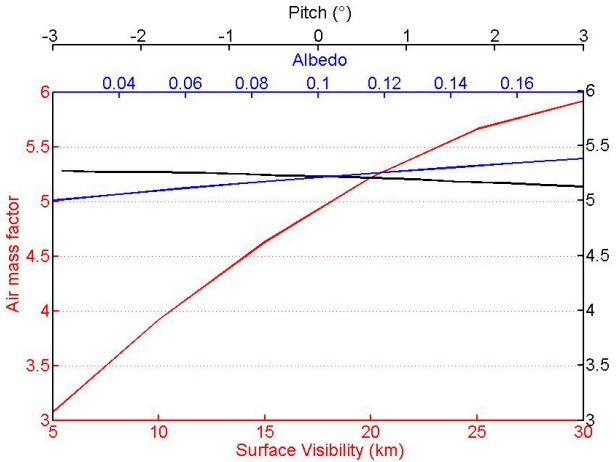

Fig. 6. Air mass factor versus surface visibility (red), albedo (blue) and pitch angle (black). The last two parameters only have small effects due to the limb observation's geometry and the large field-of-view, respectively.

AMTD
5, 1947–1984, 2012

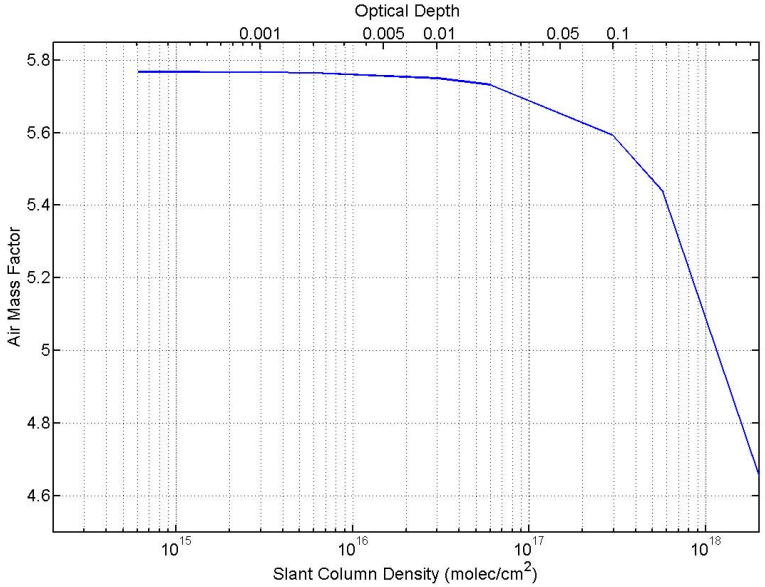

Fig. 7. Air mass factor versus slant column density. NO_2 loading start to influence significantly the radiative transfer above 5×10^{16} molec cm^{-2}.

AMTD
5, 1947–1984, 2012

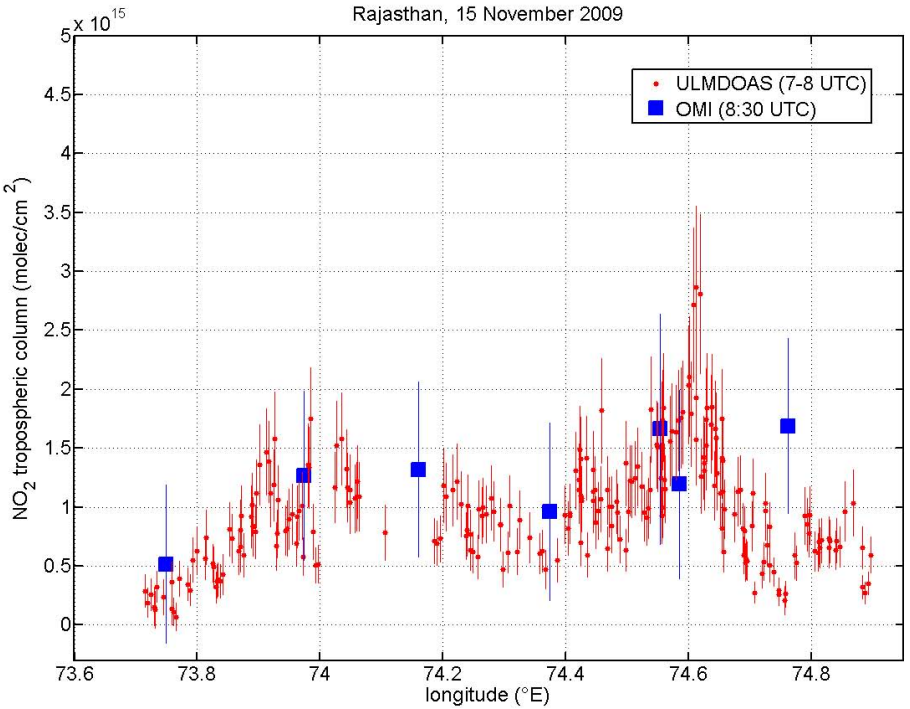

Fig. 8. ULMDOAS (red) and OMI (blue) measurements over Rajasthan, India (15 November 2009). The NO_2 field is rather uniform.

AMTD
5, 1947–1984, 2012

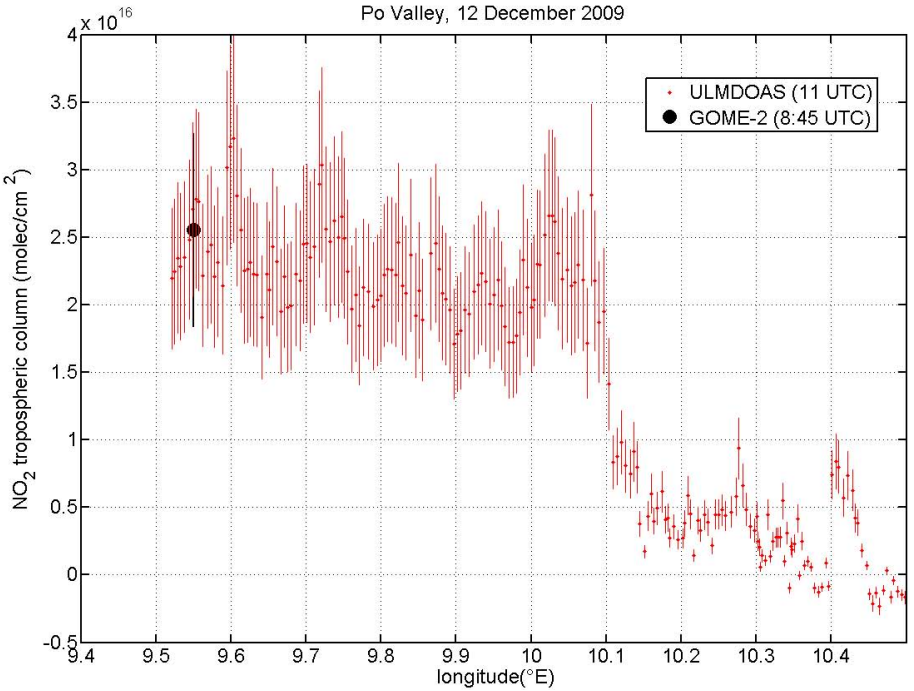

Fig. 9. ULMDOAS (red) and GOME-2 (blue) measurements over Italy (2 December 2009). The zone East of 10° E is the Po Valley.

AMTD
5, 1947–1984, 2012

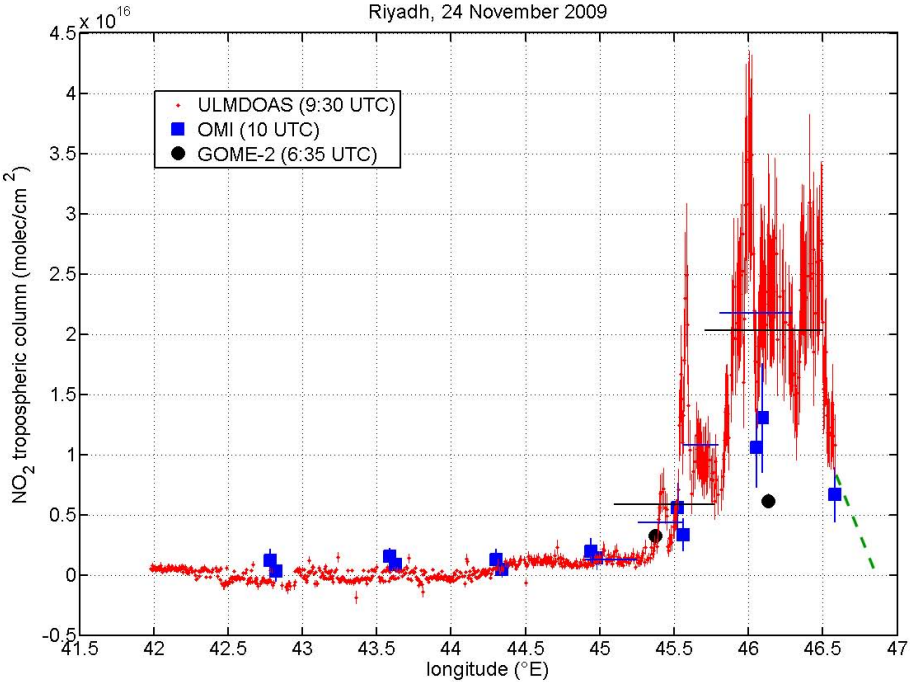

Fig. 10. ULMDOAS (red), OMI (blue), and GOME-2 (black) measurements over Riyadh (24 November 2009). Horizontal blue and black lines correspond to ULMDOAS data averaged over OMI and GOME-2 pixel extensions, respectively. ULMDOAS tropospheric NO_2 measurements are larger in this case than the one seen by both satellites.

AMTD
5, 1947–1984, 2012

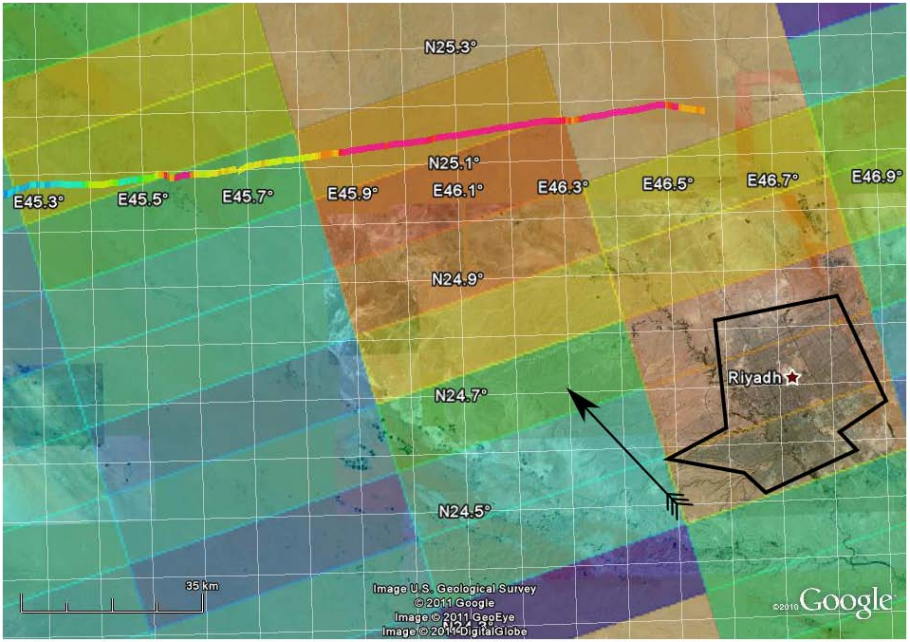

Fig. 11. Map of Riyadh surrounding with ULMDOAS and OMI NO_2 data superimposed. Riyadh agglomeration is delimited by the black polygon. The arrow indicate the wind direction according to GDAS archive.

AMTD
5, 1947–1984, 2012

Fig. 12. Picture of Chittagong ship cemetery taken during the expedition. The visibility is obviously low. Courtesy Michel de Maegd.

AMTD
5, 1947–1984, 2012

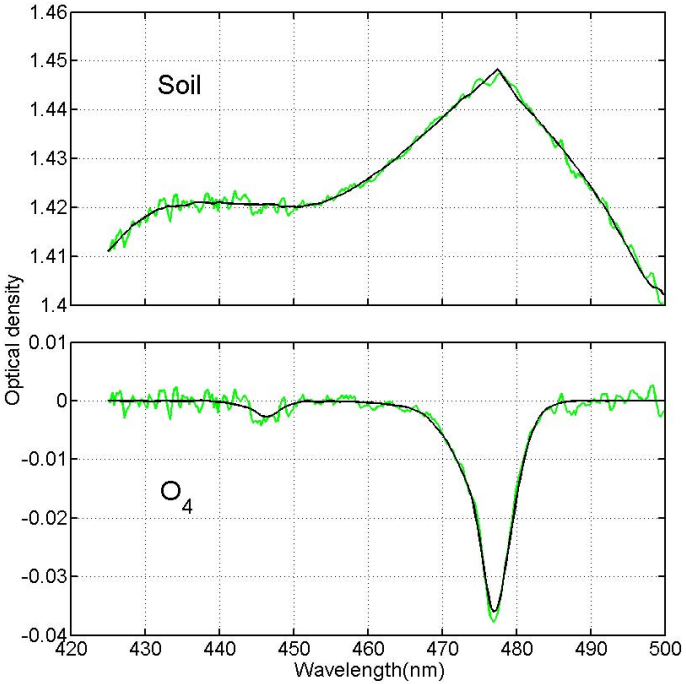

Fig. 13. Soil signature in the spectra in the Saudi Arabia desert (upper panel). For comparison, the O_4 signature displayed on the lower panel.

AMTD
5, 1947–1984, 2012

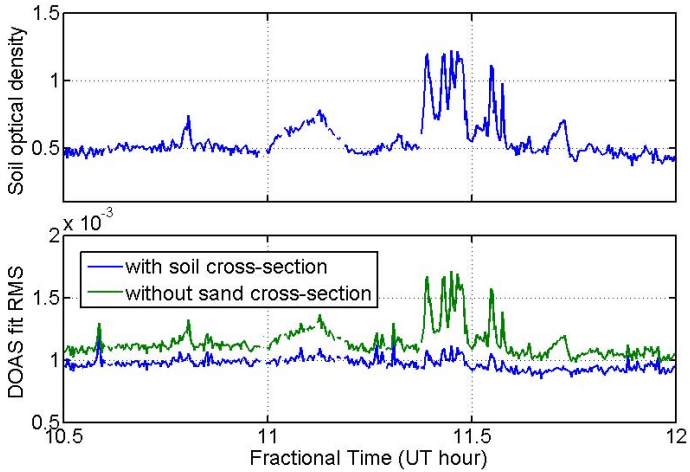

Fig. 14. Time series of the soil signature signal (upper panel) and root mean square of the DOAS fit (lower panel), including (blue curve) or not (green curve) this soil signature in the fit. The spectra were recorded above Saudi Arabia when the pilots reported their crossing of a sand storm.

AMTD
5, 1947–1984, 2012